Furukawa et al. *NPG Asia Materials* (2024)16:2
https://doi.org/10.1038/s41427-023-00522-8

NPG Asia Materials

ARTICLE Open Access

Mode-dependent magnonic noise

Ryo Furukawa[1], Shoki Nezu[1], Takuro Eguchi[1] and Koji Sekiguchi[2,3]

Abstract

The performance of magnonic devices such as converters, switches, and multiplexers greatly depends on magnonic noise. While a peculiar discrete magnonic noise has been previously reported, the sources of underlying magnon dynamics occurring in high-magnon density conditions have not been clarified. Here, zero-span measurements of the spectrum analyzer were recorded to accurately detect magnonic noise as a fluctuation of the spin-wave amplitude. The results of low-frequency magnonic noise demonstrated a spin-wave mode dependency, indicating the existence of a peculiar magnon surface state. Furthermore, the energy thresholds of four-magnon scattering and autooscillation were determined using magnonic white noise. The noise data obtained in this study can help promote theoretical and experimental research on magnons.

Introduction

Magnonics offers a new class of next-generation information processing, namely, spin-wave computing[1–7]. Magnons, the quanta of spin waves, are noncharged information carriers used to develop magnonic functionalities such as magnon transistors[8], multiplexers[9], logic circuits[10–12], switches[13], and converters[14]. Noncharged magnons release information processing devices from electronic Joule heating and broaden the material design, including even electric insulators. Development of an unconventional electronic/magnonic combined device is possible if an efficient technique for electronic-magnonic transformation is established. However, the fundamental performance capability of these magnonic devices is limited by noise, similar to electronic complementary metal–oxide–semiconductor (CMOS) devices[15,16]. For example, magnon logic and switches require a high on/off ratio to realize robust operation, and the on/off ratio depends on destructive phase interference[17,18], which is significantly affected by spin-wave amplitude fluctuations. Considering the application viewpoint as well as fundamental physics, noise provides significant information about carrier dynamics. For example, electronic $1/f$ noise reflects the carrier trapping and emission processes from the surface electron states of defects[19]. Furthermore, electronic shot noise provides insight into the carrier transmission process in a potential barrier[20]. Thermal (Jones–Nyquist) noise provides insight into the random agitation of carriers. Quantum shot noise in a two-dimensional electron gas (2DEG) provides insight into the effect of quantum statics (fermions or bosons)[21] on the carrier transmission process. Therefore, magnonic noise measurements are considered essential for optimal construction of robust magnonic devices and understanding of magnon dynamics.

Significant research has been conducted on magnonic noise in backwards-volume magnetostatic waves (BVMSWs) and magnetostatic surface spin waves (MSSWs) using a single magnonic waveguide[22]. Studies have been performed using a low-barrier Schottky diode to detect low-frequency amplitude fluctuations, where the faint fluctuation signal was amplified using a low-noise amplifier. Other studies show that the low-frequency amplitude noise of magnons is dominated by random telegraph signal (RTS) noise, and magnons in BVMSWs produce less noise than those in MSSWs. These results raise the question of how magnon (boson) noise differs from electron (fermion) noise[23,24]. Discrete RTS noise is created when several magnons disappear during a single step in the RTS signal. However, it is uncertain whether

Correspondence: Koji Sekiguchi (sekiguchi-koji-gb@ynu.ac.jp)
[1]Graduate School of Engineering Science, Yokohama National University, Tokiwadai 79-5, Yokohama 240-8501, Japan
[2]Institute of Advanced Science, Yokohama National University, Tokiwadai 79-5, Yokohama 240-8501, Japan
Full list of author information is available at the end of the article
These authors contributed equally: Ryo Furukawa, Shoki Nezu

boson-bunching-like behavior can be detected in such high-magnon density conditions ($n_M \sim 2\times 10^{17} cm^{-3}$). Further studies on low-frequency noise are needed.

In this study, we recorded highly accurate noise measurements using the zero-span operation of a spectrum analyzer. In contrast with previous studies, our proposed method excludes electronic noise resources such as electronic amplifiers and electronic Schottky diodes, which contain electronic contributions contributing noise that is difficult to separate from the magnonic noise signal. Furthermore, we introduced a permanent magnet system instead of electromagnets that induce strong spike noise originating from the electronic switching power regulator and destroy the true evaluation of magnonic noise (see supplemental material). Thus, low-frequency and white magnonic noises were clearly detected. Additionally, we demonstrated that low-frequency magnonic noise does not include RTS noise and shows $1/f^{\alpha}$ dependence on the magnon current, where α is an index number. The index α of BVMSWs is small and approaches the index of MSSWs, asymptotically depending on the increase in the magnon density. Notably, because our proposed method is sensitive to the threshold value of four-magnon scattering and autooscillation (AO), it can be used to investigate the magnon state and magnon dynamics in magnonic devices.

Results and discussion

The spin-wave waveguide (magnon conductor) used was a ferrimagnetic yttrium iron garnet (YIG) film with a thickness of $t = 10\,\mu m$. The YIG film was grown using INNOVENT e.V. Technologieentwicklung Jena (Germany). The length and width of the waveguide were 20 mm and 2 mm, respectively, and the edges of the waveguide were cut at a 45° angle to prevent edge scattering. As shown in Fig. 1, spin waves (magnon current) were generated by an excitation antenna comprising a 450 μm wide microwave strip line connected to a signal generator (Agilent Technology 83732 B). The other end of the antenna was connected to a low-noise ground line (GND). The spin-wave signal was detected by an antenna comprising a 75-μm wide microwave strip line connected to a spectrum analyzer (Agilent Technology E4440A). The optimal distance between the antennas, that is, the propagation length of the spin waves, was 4 mm. The YIG film allows the long-distance propagation of spin waves over 10 mm, and the antenna distance changes the effect of direct electromagnetic interference (EMI) between antennas. These characteristics are crucial for accurately evaluating the spin-wave amplitude, which is evaluated as an induced voltage on the antenna. If the antennas are close to each other, the EMI-induced voltage dominates the signal. Conversely, if the antennas are too separated, then the spin-wave amplitude will be too attenuated by magnetic damping. The basic BVMSW and MSSW propagation characteristics in the fabricated YIG film were measured; the results are summarized in the supplemental material. An external magnetic field $H_x = 66.0\,kA/m$ (830 Oe) was applied parallel to the waveguide (x-direction) to generate BVMSWs[25], whereas $H_y = 68.4\,kA/m$ (860 Oe) was applied normally to the waveguide (y-direction) to generate MSSWs. A pair of permanent magnets was used to eliminate unfavorable EMI from the power supply of the electromagnet.

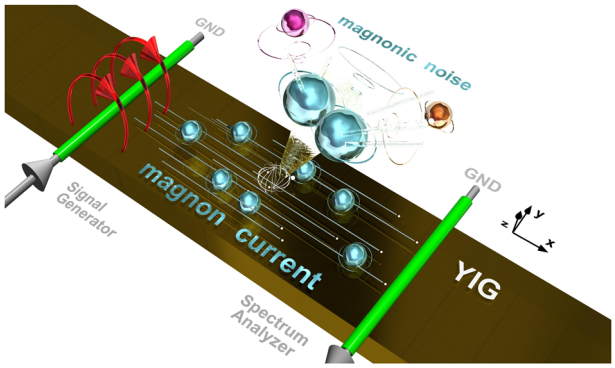

Fig. 1 Schematic of the magnonic noise measurement. Schematic of the proposed magnonic device architecture. The excitation frequencies of the spin waves are $f = 4.0900$ GHz for BVMSWs and $f = 4.2110$ GHz for MSSWs, and an external magnetic field is applied along the x- and y-directions for BVMSWs and MSSWs, respectively. Magnonic noise is detected by a pair of antennas above a YIG waveguide with the zero-span operation of the spectrum analyzer.

To obtain the magnonic noise signal, the excitation frequencies of BVMSWs and MSSWs were fixed at $f_p = 4.0900$ GHz and $f_p = 4.2110$ GHz, respectively. The local oscillator (LO) of the spectrum analyzer remained fixed at these frequencies, and zero-span measurements were performed under these conditions. The zero-span signal V(t) comprised spin-wave amplitude V_{sw} and magnonic noise, as represented by $V(t) = V_{SW} + \Delta V_{noise}(t)$. The spin-wave amplitude V_{sw} (magnitude of the magnon current) was determined using the mean value $\overline{V(t)}$.

As shown in Fig. 2, magnonic noise appeared in both BVMSWs and MSSWs. Figure 2(a) shows that magnonic noise was observed as a fluctuation of the spin-wave amplitude in the zero-span measurement. At a relatively weak excitation power $P_{in} = 0$ dBm, the fluctuation of $V(t)$ of the MSSWs, indicated by red squares, was stronger than that of the BVMSWs, indicated by the blue squares. The mean value of $\overline{V(t)}$ $(=V_{sw})$ of MSSW was 7.3 mV, and the standard deviation was $\sigma = 4.2\times 10^{-6}$. The mean value of $\overline{V(t)}$ $(=V_{sw})$ of the BVMSWs was 1.3 mV, and the standard deviation was $\sigma = 1.3\times 10^{-6}$. The standard deviation is considered a suitable parameter for comparing the magnitude of $\Delta V_{noise}(t)$. To examine the

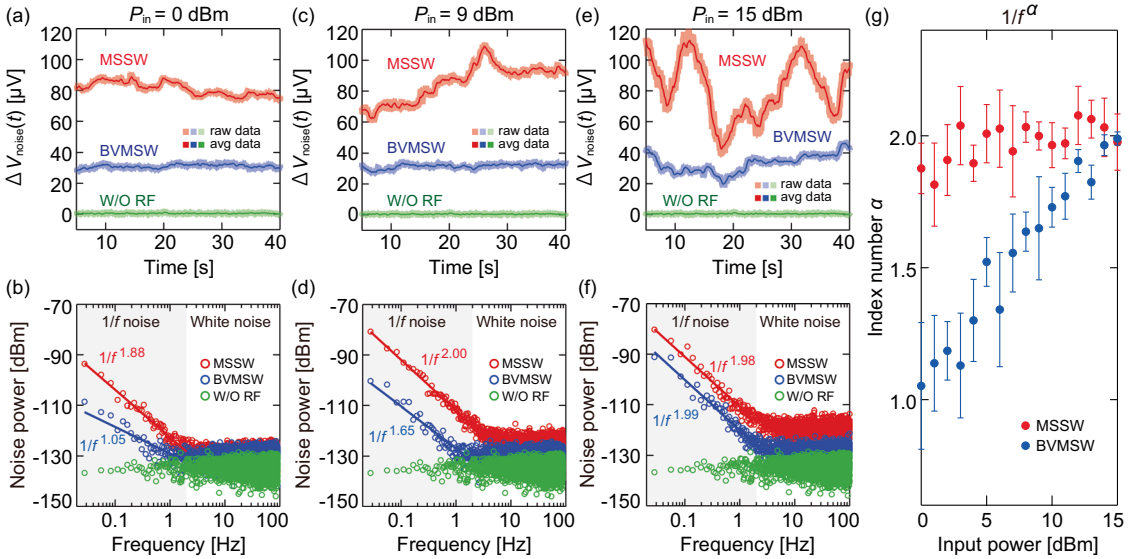

Fig. 2 Evolution of low-frequency magnonic noise. a Spin-wave amplitude fluctuations *V*(t) of BVMSWs and MSSWs at an excitation power $P_{in} = 0$ dBm. The signals are offset. **b** Power spectra of amplitude fluctuations. Low-frequency noise is fitted using the function $1/f^{\alpha}$. **c** Spin-wave amplitude fluctuations at $P_{in} = 9$ dBm. **d** Their power spectra. **e** Spin-wave amplitude fluctuations at $P_{in} = 15$ dBm. **f** Their power spectra. **g** Power dependence of the low-frequency magnonic noise index.

contribution of background noise, the reference signal was measured without microwave (RF) injection, as indicated by the green squares; the electronic noise in our system was shown to be negligible. The power spectrum of the magnonic noise was determined by calculating the fast Fourier transform (FFT), as shown in Fig. 2b. The background system noise was −135 dBm and remained unchanged over the entire frequency region. At a higher frequency of $f > 2$ Hz, the noise spectra of the BVMSWs and MSSWs became constant (white noise) at −130 dBm, as calculated by averaging the values from 10 Hz to 100 Hz. At a lower frequency of $f < 2$ Hz, the noise spectra showed $1/f^{\alpha}$ dependences, where α is an index number. Based on fitting, the index numbers for the BVMSWs and MSSWs were obtained as $\alpha = 1.05$ and $\alpha = 1.88$, respectively.

The magnonic noise $\Delta V_{noise}(t)$ became stronger when the excitation power was increased to $P_{in} = 9$ dBm. As shown in Fig. 2c, the mean value of $\overline{V(t)}$ $(=V_{sw})$ of MSSW was 20 mV, and the standard deviation was $\sigma = 1.2 \times 10^{-5}$. Similarly, the mean value of $\overline{V(t)}$ $(=V_{sw})$ of the BVMSWs was 3.6 mV, and the standard deviation was $\sigma = 1.6 \times 10^{-6}$. As shown in Fig. 2d, the noise spectra of the BVMSWs at $f < 2$ Hz were enhanced to an index $\alpha = 1.65$, whereas that of MSSW was almost unchanged ($\alpha = 2.00$). At a stronger excitation power of $P_{in} = 15$ dBm, as shown in Fig. 2e, the mean value of $\overline{V(t)}$ $(=V_{MSSW})$ was 34 mV, and the standard deviation was larger ($\sigma = 1.9 \times 10^{-5}$), whereas the mean value of $\overline{V(t)}$ $(=V_{BVMSW})$ was 7.1 mV, and the standard deviation was $\sigma = 5.8 \times 10^{-6}$. The index numbers of BVMSWs and MSSWs were $\alpha = 1.99$ and 1.98, respectively. As shown in Fig. 2f, the standard deviation increased as the excitation power increased for both spin-wave modes. The standard deviation corresponded to the magnitude of fluctuation, indicating that the spin wave became unstable. Therefore, the population of magnons fluctuated. Figure 2g shows the power dependence of the index α of the low-frequency magnonic noise $1/f^{\alpha}$. The index α of BVMSWs increased significantly from 1.0 to 2.0, whereas that of MSSW remained unchanged at approximately 2.0.

Notably, α could indicate the magnon dynamics at the surface of the YIG waveguide. In CMOS devices, $1/f^{\alpha}$ noise originates from the surface carrier (electron) states[26–28]. Similarly, as reported previously[29], a harshened YIG surface increases the low-frequency spectrum, revealing the effect of the surface state. Therefore, the enhancement of α in the BVMSWs can reflect the increased contribution of the magnonic surface state (magnon scattering), or, in the word of fluid dynamics, spin-wave turbulence[30] at the surface. As shown in Fig. 3, the BVMSWs could change their spatial distribution owing to high-power excitation. The excited BVMSWs at a lower power were mainly distributed in the central region of the YIG waveguide, as shown in Fig. 3a. However, as the excitation power increased, the BVMSWs encountered internal turbulence and broadened the spatial distribution toward the surface [Fig. 3b]. The BVMSWs is then subjected to strong surface turbulence, similar to the case of a normal fluid, such as water.

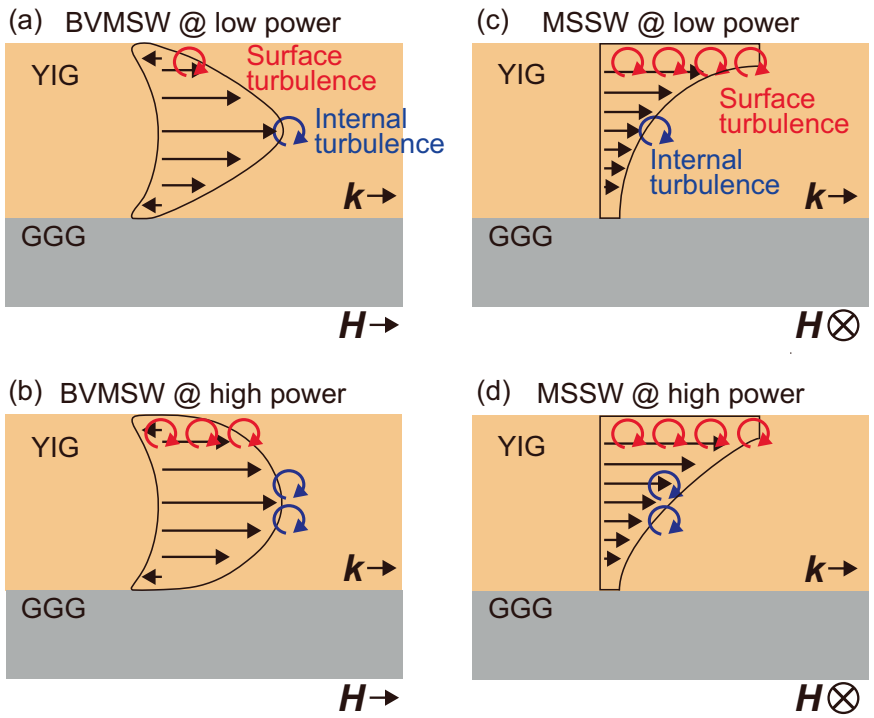

Fig. 3 Evolution of the spatial distribution of spin waves. Schematic profiles of the spin-wave density and group velocity of **a** BVMSW and **c** MSSW at a lower excitation power. Profiles of the spin-wave potential and group velocity of **b** BVMSW and **d** MSSW at a higher excitation power. Owing to the increase in internal turbulence, the spatial distribution of the spin wave expands toward the YIG surface.

Conversely, the spatial distribution of the MSSW remained almost unchanged by the excitation power owing to the well-known nonreciprocal magnetic potential, and the contribution of surface turbulence was always higher than that of internal turbulence [Fig. 3c, d].

To better understand the mechanism of magnon turbulence (scattering), micromagnetic simulations were performed (see METHODS section for details regarding the parameters). The magnitude of the external magnetic field was fixed at 67.6 A/m (850 Oe). We conducted a simulation with a 10 ns excitation sinusoidal pulse, and the spin-wave propagation was visualized as a wave packet in the time domain. The spin waves were excited at simulation position $x = -0.3$ mm and detected at simulation position $x = 0.3$ mm. As shown in Fig. 4a, in the BVMSWs ($\boldsymbol{k} \parallel \boldsymbol{M}$), the excitation pulse ($h_{\mathrm{rf}} = 766$ A/m) generated two clear spin-wave wavefronts at $t = 20$ ns propagating in the positive ($x > 0$) and negative ($x < 0$) directions. The depth profile of the wavefront was uniform on this color scale. Furthermore, the depth dependence of the spin-wave amplitude was analyzed using the spin-wave packets at the surface (x, z) = (0.3 mm, +4.25 μm) and at the center (x, z) = (0.3 mm, +0.25 μm). As shown in Fig. 4b, the spin waves showed approximately identical wave packets. The frequency dispersion of the spin-wave wave packet was deduced by the FFT power spectrum $P(f)$ over 10 ns < t < 50 ns, as shown in Fig. 4c, thereby proving that the coherence is almost unchanged by the propagation depth. To examine the experimental data, magnon intensity was calculated by the FFT power spectrum (the integrated intensity $\int_{2\,\mathrm{GHz}}^{6\,\mathrm{GHz}} P(f)df$ over gray-colored region 2 GHz < f < 6 GHz), and the excitation field (h_{rf}) dependence of magnon intensity is shown in Fig. 4d. Notably, Fig. 4d shows normalized magnon intensities. The intensities showed distinct "bullet" profiles, as depicted in Fig. 3a. Moreover, the evolutions of the profiles are shown in Fig. 3b. The magnon intensity at the surface ($z = +4.25$ μm) increased as the excitation power increased. The same micromagnetic analysis was performed for MSSW ($\boldsymbol{k} \perp \boldsymbol{M}$). Figure 4e–g show that the wave propagations were coherent both at surface (x, z) = (0.3 mm, +4.25 μm) and at center (x, z) = (0.3 mm, +0.25 μm). As shown in Fig. 4h, the magnon intensity at the surface ($z = +4.25$ μm) was stronger than that at the bottom interface ($z = -4.25$ μm), and the profile reproduced the nonreciprocal feature exactly, as shown in Fig. 3c. The magnon intensity at the center region increased as the excitation power increased [Fig. 3d].

The effect of magnon turbulence (scattering) was simulated by introducing two different types of grooves at the YIG surface: periodic grooves [Fig. 5a–j)] and random grooves [Fig. 5k–t] with a groove depth of 0.5 μm. As

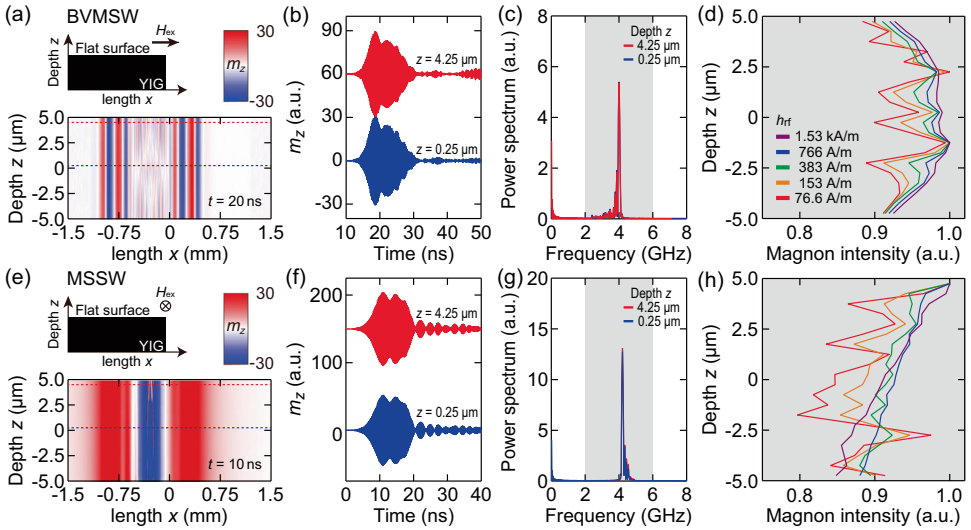

Fig. 4 Micromagnetic analysis of the depth profile of magnon density. Depth profiles of spin-wave wavefronts at $h_{rf} = 766$ A/m for **a** BVMSW and **e** MSSW. The calculation is performed with a flat surface. The spin-wave packets in the time domain at the surface and center positions for **b** BVMSW and **f** MSSW. The power spectrum of the time-domain wave packet for **c** BVMSW and **g** MSSW. Excitation-field dependences of the normalized magnon intensity for **d** BVMSW and **h** MSSW.

shown in Fig. 5a, b, the BVMSW amplitude (at $h_{rf} = 766$ A/m) decreased significantly at the surface ($z = +4.25$ μm). The power spectrum in Fig. 5c shows a decrease in amplitude. The normalized profile of magnon intensity was revealed by calculation, $\int_{2\,\mathrm{GHz}}^{6\,\mathrm{GHz}} P(f)df$ as shown in Fig. 5d. The frequency components 2 GHz < f < 6 GHz corresponded to the coherent waves. As shown in Fig. 5d. The periodic surface acts as magnonic crystals and reduces the spin-wave intensity from 0.88 to 0.062. At the opposite interface ($z = -4.25$ μm), the magnon intensity remained unchanged due to the flat surface, similar to that shown in Fig. 4. The reduction rate became stronger when the excitation field (h_{rf}) increased from 76.6 A/m to 1.53 kA/m. Due to the conservation law of wavevector $\boldsymbol{k}$, the reduced components of spin waves should be transformed into different frequency components. To verify the occurrence of this transformation, the integrated intensities of the power spectra ($\int_{0\,\mathrm{GHz}}^{2\,\mathrm{GHz}} P(f)df$) were calculated as shown in Fig. 5e. Noncoherent magnon intensities were strongly enhanced near the surface ($z = 3$ μm), indicating spin-wave backflow from surface turbulence (scattering): magnons were scattered at the groove and entered back into the central region as the excitation power increased. The MSSWs showed marked differences from the BVMSWs. As shown in Fig. 5f–h, the MSSW packet showed a smaller decrease in amplitude at $h_{rf} = 766$ A/m and a decrease in intensity from 1.0 to 0.35. The coherent components at the surface survived more than did the BVMSWs. The integrated intensities of low-frequency components ($\int_{0\,\mathrm{GHz}}^{2\,\mathrm{GHz}} P(f)df$) were calculated and are illustrated in Fig. 5j; evidently, the low-frequency components were uniformly distributed over the depth direction. Consequently, the excitation power (field) caused internal turbulence (scattering).

Considering a random groove, the same analysis was performed for BVMSWs [Fig. 5k–o] and for MSSWs [Fig. 5p–t]. The random groove is a more realistic condition than a perfect periodic groove and generates a moderate reduction in coherent components of spin waves. As shown in Fig. 5n, s, as the excitation field increased at the surface, the magnon intensity $\int_{2\,\mathrm{GHz}}^{6\,\mathrm{GHz}} P(f)df$ decreased from 0.88 to 0.18 for BVMSWs and 1.0 to 0.70 for MSSWs. Compared to the periodic groove, the low-frequency components $\int_{0\,\mathrm{GHz}}^{2\,\mathrm{GHz}} P(f)df$ showed different characteristics. The backscattered magnons were randomly distributed in the depth direction for both BVMSWs and MSSWs. These random profiles of noncoherent magnons can be the source of the experimentally observed low-frequency magnonic noise $1/f^{\alpha}$, given that the specific distribution of backscattered magnons as observed in periodic groove conditions may cause a specific frequency contribution. However, the detailed formulation of magnonic noise using this random noncoherent magnon contribution is beyond the scope of this study and remains to be elucidated. Even so, this systematic micromagnetic analysis revealed that coherent magnons encounter surface turbulence (scattering) at the surface grooves and that the successive generation of noncoherent magnons brings about a random spatial distribution over the depth direction.

The magnonic noise at $f > 10$ Hz is also sensitive to internal spin-wave turbulence. As shown in Fig. 6a, the

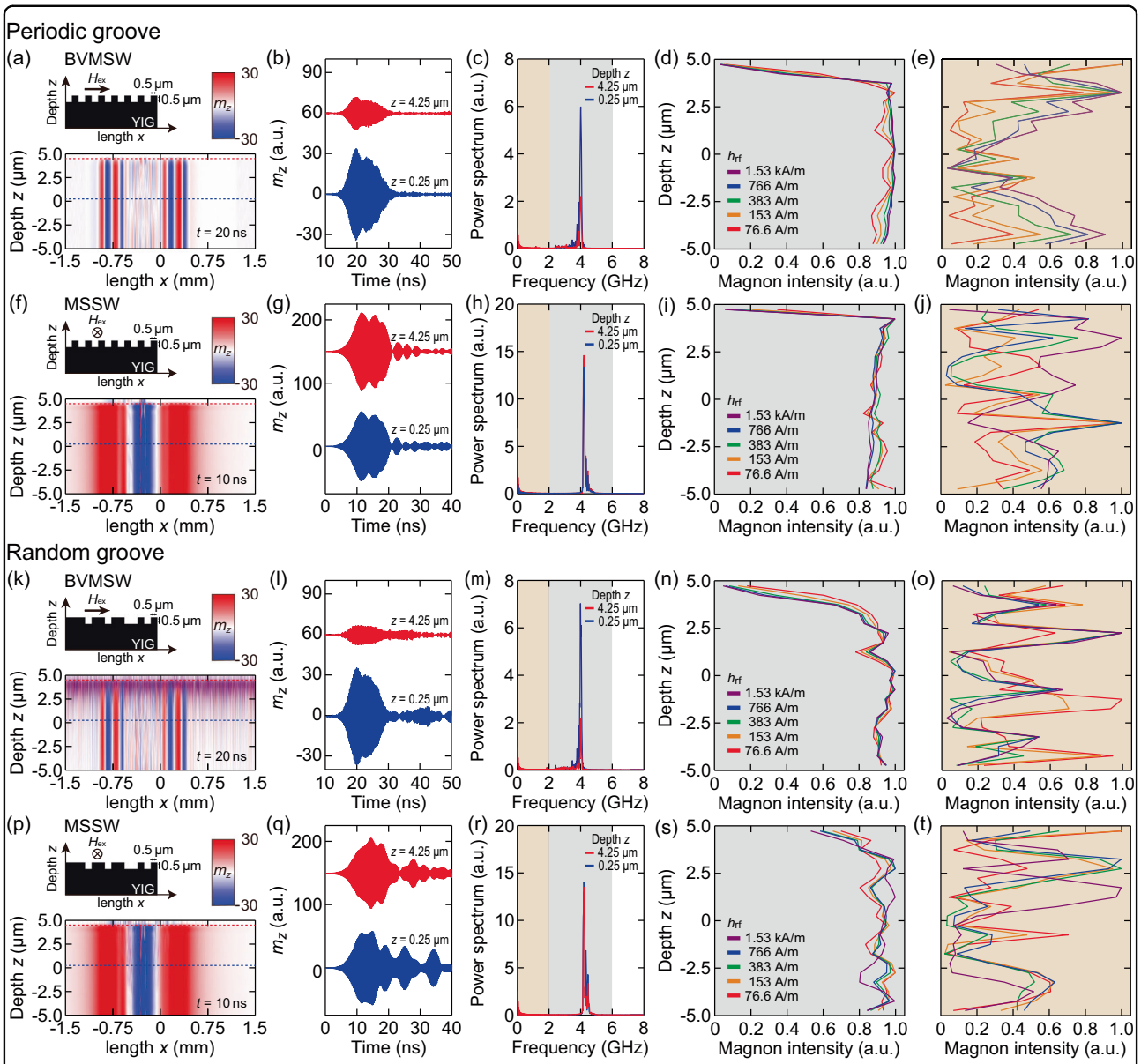

Fig. 5 Effect of surface turbulence on the magnon density. Depth profiles of spin-wave wavefronts at $h_{rf} = 766$ A/m for **a** BVMSW and **f** MSSW calculated with a periodic groove at the surface. The spin-wave packets in the time domain at the surface and center positions for **b** BVMSW and **g** MSSW. The power spectrum of the time-domain wave packet for **c** BVMSW and **h** MSSW. Excitation-field dependences of the normalized magnon intensity calculated in the frequency range 2 GHz < f < 6 GHz (gray-colored area) for **d** BVMSW and **i**. MSSW. Excitation-field dependences of the normalized magnon intensity calculated in the frequency range 0 GHz < f < 2 GHz (light yellow area) for **e** BVMSW and **j** MSSW. Depth profiles of spin-wave wavefronts at $h_{rf} = 766$ A/m for **k** BVMSW and **p** MSSW calculated with a random groove at the surface. The spin-wave packets in the time domain at the surface and center positions for **l** BVMSW and **q** MSSW. The power spectrum of the time-domain wave packet for **m** BVMSW and **r** MSSW. Excitation-field dependences of the normalized magnon intensity calculated in the frequency range 2 GHz < f < 6 GHz (gray-colored area) for **n** BVMSW and **s** MSSW. Excitation-field dependences of the normalized magnon intensity calculated in the frequency range 0 GHz < f < 2 GHz (light yellow area) for **o** BVMSW and **t** MSSW.

baseline of white magnonic noise in the MSSW increased as the excitation power increased. Moreover, the baseline of $P_{in} = 14.6$ dBm decreased from the baseline of $P_{in} = 14.2$ dBm. Strikingly, the white magnonic noise spectrum at $P_{in} = 14.2$ dBm [Fig. 6a] contained multiple peaks up to 500 kHz. To investigate this phenomenon, the noise power was calculated by averaging the spectrum over 10 Hz < f < 500 Hz, as shown in Fig. 6b. The spin-wave amplitude V_{MSSW} increased continuously, as indicated by the blue closed circles. As indicated by the red closed circles, the magnonic noise initially increased continuously; however, the noise profile exhibited

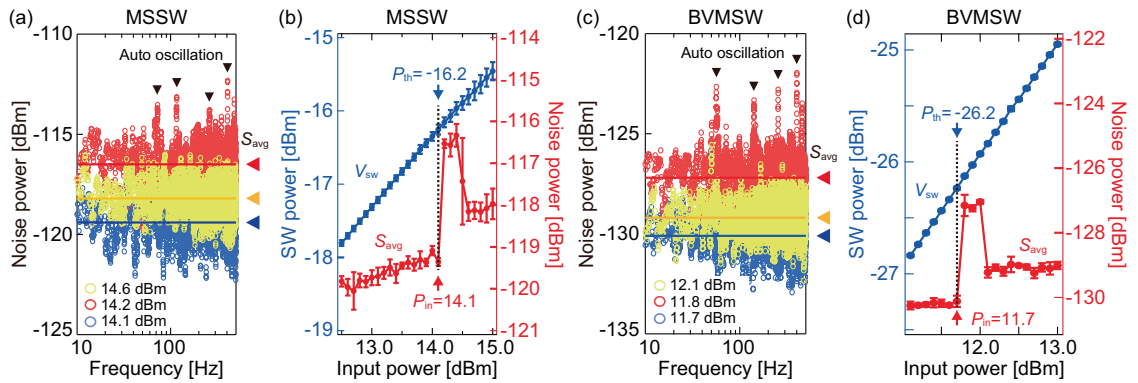

Fig. 6 Magnonic noise at a higher frequency region *f* > 10 Hz. a Excitation-power dependence of the magnonic noise spectra of the MSSW. The baseline of the white-noise region changes as the excitation power increases. **b** Noise power of the MSSW as a function of excitation power. The magnonic noise shows a discrete change at $P_{in} = 14.1$ dBm, whereas the spin-wave amplitude linearly increases as the excitation power increases. **c** Excitation-power dependence of magnonic noise spectra of BVMSWs. The baseline of the white-noise region changes as the excitation power increases. **d** Noise power of the BVMSW as a function of the excitation power. The noise shows a discrete change $P_{in} = 11.7$ dBm, whereas the spin-wave amplitude linearly increases as the excitation power increases.

discontinuous changes at $P_{in} = 14.1$ dBm and 14.6 dBm. In the case of large-amplitude spin waves, magnon-magnon scattering became stronger and caused complicated phase interference coupled with excited magnons. The number of magnons (V_{MSSW}) increased with the spin-wave instability (internal turbulence). Under these conditions, the magnonic system shows collective oscillations and multiple spectrum peaks of spin-wave AO[31–33]. The noise experiment directly yielded the threshold of energy flux in spin waves as $P_{AO}^{MSSW} = -16.2$ dBm. The abrupt change in the magnonic noise was the fingerprint of internal spin-wave turbulence. Above $P_{in} = 14.6$ dBm, the system could turn into a metastable state, and the noise spectrum could lose the AO peaks, or the AO frequency could shift toward a higher frequency[31] ($f > 500$ Hz) and disappear from the detection frequency range (10 Hz < f < 500 Hz).

Figure 6c shows the noise spectra at $f > 10$ Hz for the BVMSWs. As indicated by the red circles, the BVMSWs contain the fingerprint of AO. The power dependence of magnonic noise is shown in Fig. 6d. The magnonic noise also exhibited abrupt changes at $P_{in} = 11.7$ dBm and 12.1 dBm. Notably, the threshold energy flux $P_{AO}^{BVMSW} = -26.2$ dBm in the BVMSWs was smaller than that in the MSSWs. This phenomenon can be explained by four-magnon scattering[34–38], as discussed below.

To validate our experiment, four-magnon scattering was measured by the spin-wave spectrum using the normal operation of the spectrum analyzer with a resolution bandwidth (RBW) of 10 kHz. As shown in Fig. 7a, the MSSW spectrum exhibited specific satellite peaks near the main resonant frequency $f_p = 4.2110$ GHz. The spectral peak frequencies are listed in Table 1.

The peak frequency satisfies the relation:

$$2f_p = f_n^+ + f_n^-, \quad (1)$$

where n is the labeling number of the satellite peak. This relationship is the energy conservation law and represents the nonlinear four-magnon scattering that leads to spin-wave instability. The resonance power at f_p (number of excited magnons) and the satellite peak power at f_1^+ (number of scattered magnons) were deduced, as shown in Fig. 7b. The number of excited magnons increased continuously, while the number of scattered magnons abruptly increased at $P_{in} = 13.8$ dBm. This trend resulted in the threshold energy flux in the MSSW being $P_{4mag}^{MSSW} = -16.2$ dBm, which induced four-magnon scattering.

Similarly, the BVMSW spectrum is shown in Fig. 7c, and the peak frequencies of the BVMSW spectrum indicated by solid triangles are summarized in Table 2.

The number of satellite peaks increased, and the frequency shift $\Delta f_n = |f_n^{\pm} - f_p|$ decreased than that of MSSW; however, the energy-conservation law (four-magnon scattering) was valid for any pair of magnons. Figure 7d shows the excitation power dependence of the number of excited and scattered magnons, revealing that the threshold energy flux in the BVMSWs is $P_{4mag}^{BVMSW} = -26.4$ dBm, which induces four-magnon scattering.

Finally, we discuss the relationships between P_{4mag}^{BVMSW}, P_{4mag}^{MSSW}, P_{AO}^{BVMSW}, and P_{AO}^{MSSW}. The experimental results revealed that $P_{4mag}^{BVMSW} = -26.4\,\text{dBm} < P_{4mag}^{MSSW} = -16.2$ dBm and agreed with the theoretical frameworks of four wave processes (modulation instability[30] or second-order Suhl instability[34,39]). In general, the threshold of the oscillation amplitude $(\Delta M_z/M)_{th}$ or critical driving field h_c depends on the relative angle θ between magnetization $\boldsymbol{M}$

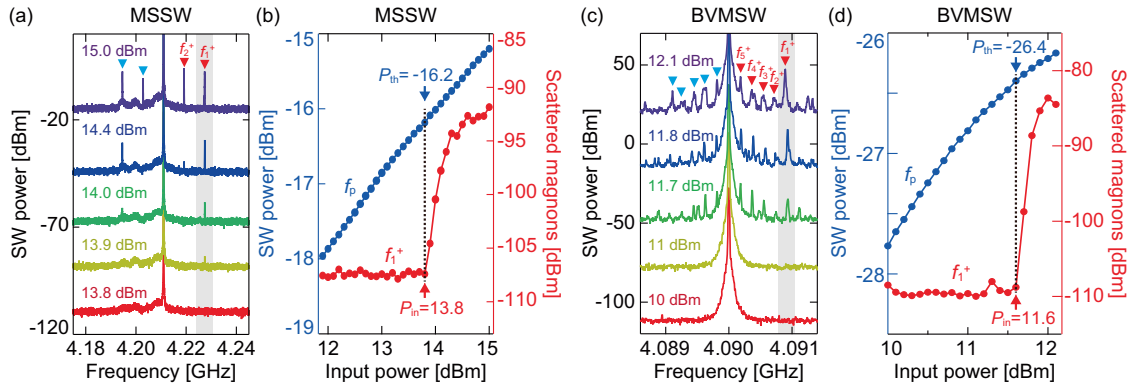

Fig. 7 Electric detection of nonlinear four-magnon scattering. a Excitation-power dependence of the MSSW resonance spectrum. The side spectrum peaks indicated by solid triangles owing to four-magnon scattering appear according to the increase in the excitation power. **b** Power dependence of the magnitude of a satellite peak at $f_1^+ = 4.2274$ GHz. The magnitude of the satellite peak abruptly increases at $P_{in} = 13.8$ dBm, whereas the excited spin-wave peak at $f_p = 4.2110$ GHz continuously increases. **c** Excitation-power dependence of the BVMSW resonance spectrum. Multiple satellite peaks owing to four-magnon scattering appear according to the increase in the excitation power. **d** Power dependence of the magnitude of a satellite peak at $f_1^+ = 4.0909$ GHz. The magnitude of the peak abruptly increases at $P_{in} = 11.6$ dBm, whereas the excited spin-wave peak at $f_p = 4.0900$ GHz continuously increases.

Table 1 Satellite-peak frequencies in MSSW ($f_p = 4.2110$ GHz and $P_{in} = 15$ dBm).

	1st satellite $n = 1$	2nd satellite $n = 2$
f_n^+ (GHz)	4.2274	4.2192
f_n^- (GHz)	4.1946	4.2028
Δf_n (MHz) $= \lvert f_n^{\pm} - f_p \rvert$	16.4	8.2

Table 2 Satellite peak frequencies in BVMSW ($f_p = 4.0900$ GHz and $P_{in} = 12.1$ dBm).

	1st satellite $n = 1$	2nd satellite $n = 2$	3rd satellite $n = 3$	4th satellite $n = 4$	5th satellite $n = 5$
f_n^+ (GHz)	4.0909	4.0907	4.0905	4.0904	4.0902
f_n^- (GHz)	4.0891	4.0893	4.0895	4.0896	4.0898
Δf_n (MHz) $= \lvert f_n^{\pm} - f_p \rvert$	0.9	0.7	0.5	0.4	0.2

and wavevector $\boldsymbol{k}$. Both thresholds become the smallest when $\theta = 0$. The theory also predicts that instability in an MSSW ($\boldsymbol{k} \perp \boldsymbol{M}$) could be induced with a larger Δf_n than that in the case of a BVMSW ($\boldsymbol{k} \parallel \boldsymbol{M}$), which is consistent with our experimental results (Tables 1 and 2). Because four-magnon scattering (instability) occurs before AO, the relationships $P_{4mag}^{BVMSW} = -26.4\,\text{dBm} \leq P_{AO}^{BVMSW} = -26.2\,\text{dBm}$, $P_{4mag}^{MSSW} = -16.2\,\text{dBm} \leq P_{AO}^{MSSW} = -16.2\,\text{dBm}$, and $P_{AO}^{BVMSW} = -26.2\,\text{dBm} < P_{AO}^{MSSW} = -16.2\,\text{dBm}$ hold.

Conclusion

This study investigated magnonic noise as a fluctuation of the spin-wave amplitude using zero-span operation of the spectrum analyzer. The $1/f^{\alpha}$ dependence of magnonic noise was specific to the spin-wave mode (MSSW or BVMSW) and provided information about surface spin-wave turbulence or the surface magnon state. The white magnonic noise revealed the nature of internal spin-wave turbulence, i.e., the excitation-power dependence of white magnonic noise revealed the threshold of spin-wave AO. The excitation-power dependence of the spin-wave resonance revealed the emergence of four-magnon scattering before spin-wave AO. Furthermore, the noise measurements enabled direct evaluation of the energy thresholds of four-magnon scattering and AO. The experimental agreement with theoretical analysis supported the conclusion that magnonic noise is sensitive to magnon dynamics. Furthermore, the magnonic noise level was very low, and its detection was limited by the internal thermal noise of the electronic signal generator and spectrum analyzer. By introducing a carefully designed signal amplifier, the detection of magnonic noise at low magnon density (linear excitation regime) could be a future research target, considering that all magnonic devices should be operating at a power of less than −5 dBm. With the information provided herein on the noise characteristics at low magnon densities, models describing surface magnon dynamics can be formulated. Therefore, we have shown that magnonic noise

measurements can be a powerful tool for helping to design future magnonic devices.

Methods

Zero-span measurement of the spectrum analyzer

For the amplitude fluctuation measurement of spin waves, an LO of the spectrum analyzer was fixed at the spin-wave resonance frequency with an RBW of 1 MHz. To reduce the electronic noise floor of the spectrum analyzer, the video bandwidth (VBW) of the spectrum analyzer was set to 1 MHz.

Micromagnetic simulation

Micromagnetic simulations were performed by numerically solving the Landau–Lifshitz–Gilbert equation, $\partial\mathbf{m}/\partial t = -\gamma_g\mu_0\mathbf{m} \times \mathbf{H}_{\mathrm{eff}} + \alpha_G\mathbf{m} \times \partial\mathbf{m}/\partial t$. Here, $\mathbf{m}$ is the unit vector along the magnetization, $\mathbf{H}_{\mathrm{eff}}$ is the effective magnetic field including the exchange, magnetostatic, and external fields, and α_G is the Gilbert damping. The dimensions of the YIG film $= 12 \times 2.1\,\mathrm{mm} \times 10\,\mu\mathrm{m}$. The following parameters were used: number of cells $(N_x, N_y, N_z) = (24000, 1, 20)$; periodic boundary condition $(P_x, P_y, P_z) = (0, 2100, 0)$; $\alpha_G = 0.0001$; exchange stiffness constant $A_{\mathrm{ex}} = 3.7 \times 10^{-12}\,\mathrm{J/m}$; and saturation magnetization $M_S = 141\,\mathrm{kA/m}$.

Acknowledgements

This work was supported by Grants-in-Aid for Scientific Research (19H00861, 18H05346, and 22K18321) from the Japan Society for the Promotion of Science (JSPS). K.S. acknowledges the support of Grants-in-Aid for Scientific Research (20H05652).

Author details

[1]Graduate School of Engineering Science, Yokohama National University, Tokiwadai 79-5, Yokohama 240-8501, Japan. [2]Institute of Advanced Science, Yokohama National University, Tokiwadai 79-5, Yokohama 240-8501, Japan. [3]Faculty of Engineering, Yokohama National University, Tokiwadai 79-5, Yokohama 240-8501, Japan

Author contributions

R.F. and K.S. planned the experiments. R.F., T.E., and K.S. designed and prepared the samples and performed the zero-span operation and normal spin-wave resonance measurements. S.N. performed the micromagnetic simulations. R.F., S.N., T.E., and K.S. wrote the manuscript. All authors discussed the results.

Data availability

The data supporting the findings of this study are available from the corresponding author upon reasonable request.

Competing interests

The authors declare no competing interests.

Publisher's note

Springer Nature remains neutral with regard to jurisdictional claims in published maps and institutional affiliations.

Supplementary information The online version contains supplementary material available at https://doi.org/10.1038/s41427-023-00522-8.

Received: 3 April 2023 Revised: 6 November 2023 Accepted: 21 November 2023
Published online: 19 January 2024

References

1. Kruglyak, V. V., Demokritov, S. O. & Grundler, D. Magnonics. *J. Phys. D Appl. Phys.* **43**, 264001 (2010).
2. Sekiguchi, K. et al. Nonreciprocal emission of spin-wave packet in FeNi film. *Appl. Phys. Lett.* **97**, 022508 (2010).
3. Macià, F., Kent, A. D. & Hoppensteadt, F. C. Spin-wave interference patterns created by spin-torque nano-oscillators for memory and computation. *Nanotechnology* **22**, 095301 (2011). Pubmed:21258144.
4. Lenk, B., Ulrichs, H., Garbs, F. & Münzenberg, M. The building blocks of magnonics. *Phys. Rep.* **507**, 107–136 (2011).
5. Wolf, S. A. et al. Spintronics: a spin-based electronics vision for the future. *Science* **294**, 1488–1495 (2001). Pubmed:11711666.
6. Bader, S. D. & Parkin, S. S. P. Spintronics. *Annu. Rev. Condens. Matter Phys.* **1**, 71–88 (2010).
7. Sekiguchi, K. The basis of magnon transistors. *AAPPS Bull.* **28**, 2 (2018).
8. Chumak, A. V., Serga, A. A. & Hillebrands, B. Magnon transistor for all-magnon data processing. *Nat. Commun.* **5**, 4700 (2014).
9. Vogt, K. et al. Realization of a spin-wave multiplexer. *Nat. Commun.* **5**, 3727 (2014).
10. Kanazawa, N. et al. The role of Snell's law for a magnonic majority gate. *Sci. Rep.* **7**, 7898 (2017).
11. Sato, N., Sekiguchi, K. & Nozaki, Y. Electrical demonstration of spin-wave logic operation. *Appl. Phys. Express* **6**, 063001 (2013).
12. Khitun, A. G., Bao, M. & Wang, K. L. Magnonic logic circuits. *J. Phys. D Appl. Phys.* **43**, 264005 (2010).
13. Iwaba, M. & Sekiguchi, K. Spin-wave switching using dynamic magnonic crystal. *Appl. Phys. Express* **14**, 073002 (2021).
14. Eguchi, T., Nezu, S., Naemura, Y. & Sekiguchi, K. Spin-wave interconversion via thermoelectric point-contact control. *Phys. Rev. Res.* **4**, 033135 (2022).
15. Ghibaudo, G. & Boutchacha, T. Electrical noise and RTS fluctuations in advanced CMOS devices. *Microelectron. Reliab.* **42**, 573–582 (2002).
16. Haartman, M. & Östling, M. *Low-Frequency Noise in Advanced MOS Devices* (Springer, 2007).
17. Sato, N., Lee, S. J., Lee, S. W., Lee, K. J. & Sekiguchi, K. Phase stability of magnonic logic operation in microfabricated metallic wires. *Appl. Phys. Express* **9**, 083001 (2016).
18. Balynsky, M. et al. Magnonic interferometric switch for multi-valued logic circuits. *J. Appl. Phys.* **121**, 024504 (2017).
19. Hooge, F. N., Kleinpenning, T. G. M. & Vandamme, L. K. J. Experimental studies on *l/f* noise. *Rep. Prog. Phys.* **44**, 479–532 (1981).
20. Blanter, Y. M. & Büttiker, M. Shot noise in mesoscopic conductors. *Phys. Rep.* **336**, 1–166 (2000).
21. Kumar, A., Saminadayar, L., Glattli, D. C., Jin, Y. & Etienne, B. Experimental test of the quantum shot noise reduction theory. *Phys. Rev. Lett.* **76**, 2778–2781 (1996). Pubmed:10060786.
22. Rumyantsev, S., Balinskiy, M., Kargar, F., Khitun, A. & Balandin, A. A. The discrete noise of magnons. *Appl. Phys. Lett.* **114**, 0900601 (2019).
23. Kogan, S. *Electronic Noise and Fluctuations in Solids* (Cambridge Univ., 2008).
24. der Ziel, A. *Noise* (Prentice-Hall, 1954).
25. Nezu, S., Scheike, T., Sukegawa, H. & Sekiguchi, K. Propagating backward-volume spin waves in epitaxial Fe films. *AIP Adv.* **12**, 035320 (2022).
26. McWhorter, A. L. *1/f Noise and Related Surface Effects in Germanium* (MIT Lincoln Lab., 1955).
27. Sah, C. T. & Hielscher, F. H. Evidence of the surface origin of the 1/*f* noise. *Phys. Rev. Lett.* **17**, 956–958 (1966).
28. Reimbold, G. Modified 1/*f* trapping noise theory and experiments in MOS transistors biased from weak to strong inversion—Influence of interface states. *IEEE Trans. Electron Devices* **31**, 1190–1198 (1984).
29. Carroll, T. L., Pecora, L. M. & Rachford, F. J. Chaos and chaotic transients in yttrium iron garnet (invited). *J. Appl. Phys.* **64**, 5396–5400 (1988).
30. L'vov, V. *Wave Turbulence Under Parametric Excitation* (Springer, 1994).
31. L'vov, V. S., Musher, S. L. & Starobinets, S. S. Theory of magnetization self-oscillations on parametric excitation of spin waves. *Zh. Eksp. Teor. Fiz.* **64**, 1074·1086 (1973).
32. Rezende, S. M. & De Aguiar, F. M. Strange attractors in SPIN-WAVE chaos. *Phys. A* **163**, 232–247 (1990).

33. Azevedo, A. & Rezende, S. M. Controlling chaos in spin-wave instabilities. *Phys. Rev. Lett.* **66**, 1342–1345 (1991). Pubmed:10043181.
34. Sparks, M. Ferromagnetic relaxation theory (McGraw-Hill. Book 1964).
35. Schultheiss, H., Vogt, K. & Hillebrands, B. Direct observation of nonlinear four-magnon scattering in spin-wave microconduits. *Phys. Rev. B* **86**, 054414 (2012).
36. Mohseni, M. et al. Controlling the nonlinear relaxation of quantized propagating magnons in nanodevices. *Phys. Rev. Lett.* **126**, 097202 (2021). Pubmed:33750157.
37. Lee-Wong, E. et al. Nanoscale detection of magnon excitations with variable wavevectors through a quantum spin sensor. *Nano Lett.* **20**, 3284–3290 (2020). Pubmed:32297750.
38. Kazakov, G. T., Kozhevnikov, A. V. & Filimonov, Y. A. Four-magnon decay of magnetostatic surface waves in yttrium iron garnet films. *Phys. Solid State* **39**, 288–295 (1997).
39. Suhl, H. The theory of ferromagnetic resonance at high signal power. *J. Phys. Chem. Solids* **1**, 209–227 (1957).